



# Helium distributions in ocean island basalt olivines revealed by X-ray computed tomography and single-grain crushing experiments

Forrest Horton<sup>a,\*</sup>, Kenneth Farley<sup>b</sup>, Matthew Jackson<sup>c</sup>

<sup>a</sup> Woods Hole Oceanographic Institution, Geology & Geophysics, 360 Woods Hole Rd, McLean, MS #08, Woods Hole, MA 02543, United States

<sup>b</sup> Division of Geological and Planetary Sciences, California Institute of Technology, MC 170-25, Pasadena, CA 91125, United States

<sup>c</sup> Department of Earth Science, 1006 Webb Hall, University of California, Santa Barbara, CA 93106-9630, United States

Received 30 April 2018; accepted in revised form 12 October 2018; Available online 28 October 2018

## Abstract

X-ray computed tomography of individual olivine crystals in basalts from Ofu and Olosega islands, American Samoa, reveals that a small fraction of the olivines contain the vast majority of the fluid inclusions. Single-grain crushing experiments demonstrate that He and CO<sub>2</sub> reside primarily in these inclusions. Low CO<sub>2</sub> pressures in most grains, corresponding to depths of less than 1 km, provide evidence of ubiquitous decrepitation and associated pressure reduction in the fluid inclusions. Even so, the olivines with the highest inclusion volumes yielded sufficient He to obtain precise He concentrations and isotopic compositions. Within analytical uncertainty, <sup>3</sup>He/<sup>4</sup>He ratios are homogeneous among the olivines from each basalt, but among basalts, the ratios range from 21 to 35 Ra. The total range in C/<sup>3</sup>He ratio within the analyzed olivines is from  $3.6 \times 10^7$  to  $1.5 \times 10^{10}$ , and varies by nearly an order of magnitude within the olivines from each basalt. We postulate that this wide range of C/<sup>3</sup>He ratios is caused by grain-scale decoupling of C and <sup>3</sup>He due to extensive He diffusion out of fluid inclusions through the olivine lattice during magma ascent and cooling. If so, primary Ofu-Olosega magmas probably had C/<sup>3</sup>He ratios less than  $4 \times 10^8$ , which is lower than previous estimates for hotspot magmas.

© 2018 Elsevier Ltd. All rights reserved.

**Keywords:** Olivine-hosted fluid inclusions; Helium diffusion; Carbon-to-helium ratios; X-ray computed tomography

## 1. INTRODUCTION

The isotopic composition of He carried in basaltic magmas is diagnostic of mantle origins. Chemically inert and scarce in Earth's atmosphere, He is neither susceptible to significant isotopic fractionation nor to atmospheric contamination during sample preparation and analysis. Nevertheless, the utility of He as a geochemical tracer is limited by the scarcity of He in geologic samples. Mantle magmas contain low concentrations of He, much of which is lost during open system degassing that occurs during eruption and

emplacement (e.g., [Gonnermann and Mukhopadhyay, 2007](#)). Submarine glasses from mid ocean ridges retain enough He to characterize the isotopic composition of the depleted upper mantle (e.g., [Javoy and Pineau, 1991](#); [Graham et al., 1992](#); [Marty and Zimmermann, 1999](#)). In hotspot magmas commonly thought to derive from the deep mantle, however, olivines are the only viable He repository, except in rare instances when submarine glasses (e.g., [Kurz et al., 1983](#); [Graham et al., 1993](#); [Kendrick et al., 2015](#)) or hydrothermal vents (e.g., [Hilton et al., 1998](#); [Botz et al., 1999](#)) can be sampled. Noble gases are extremely incompatible in olivine ([Marty and Lussiez, 1993](#); [Heber et al., 2007](#)), but can reside in olivine-hosted melt or fluid inclusions. On average, ocean island basalt (OIB) olivines

\* Corresponding author.

E-mail address: [horton@whoi.edu](mailto:horton@whoi.edu) (F. Horton).

have low He concentrations relative to analytical detection limits (e.g., Kurz et al., 1982; Farley et al., 1993; Jackson et al., 2007), necessitating the extraction of He from gram-sized mineral separates consisting of hundreds to thousands of individual crystals (Farley and Neroda, 1998). This bulk approach provides no information about the distribution of He among the crystals, so the mechanisms by which olivines entrain, retain, and exchange He during ascent and eruption are poorly understood.

To remedy this situation, we investigated individual OIB olivine crystals from picritic basalt dikes collected on Ofu and Olosega islands, American Samoa. Previous work established that bulk olivine separates from samples from this location have high and variable  $^3\text{He}/^4\text{He}$  ratios (19.5–33.8 Ra; Jackson et al., 2007). The lavas have abundant large olivines that we consider ideal for characterizing intra-grain He concentration and isotopic variability. Because He is thought to reside in fluid inclusions (e.g., Kurz et al., 1983; Poreda and Farley, 1992; Burnard et al., 1994), we used X-ray computed tomography (microCT), a non-destructive imaging technique, to measure the inclusions in olivine grains prior to He isotopic analysis. The identification of inclusion-rich grains *a priori* by microCT (Fig. 1) enabled He and  $\text{CO}_2$  characterization of individual olivines. We discovered that olivines from each sample have homogeneous He isotopic compositions, but highly variable He concentrations, internal pressures, and  $C/^3\text{He}$  ratios. Our findings suggest that volatiles trapped in OIB olivine generally do not correspond to the conditions of olivine growth.

## 2. METHODS

We analyzed eight picritic basalts collected near the Asaga Strait between Ofu and Olosega islands, the easternmost islands of the Samoan archipelago. All except two—a beach cobble (Ofu-05-23) and a landslide cobble (Ofu-05-28)—are from dikes exposed in road cuts and therefore were exposed to minimal cosmic ray irradiation that could contribute extraneous  $^3\text{He}$  to the samples. K-Ar dates of volcanic flows elsewhere on the islands are 240–440 ka (McDougall, 2010); the dikes cut these flows and are hence younger. After gently crushing the basalt samples by hand, we handpicked olivine crystals, cleaned them in ultrasonic ethanol baths, and dried them at room temperature. 1065

of the largest phenocrysts (approximately 100 from each sample, except for the most He-rich sample, Ofu-05-23, from which we selected 279 grains) were mounted on adhesive tape and stacked into cylindrical plastic capsules 1 cm in diameter and 1 cm high. These volumes were scanned with a voxel resolution of 7.18–7.85  $\mu\text{m}$  on an Xradia microCT instrument at the University of Texas high-resolution X-ray computed tomography facility.

For volume-rendering purposes, we imported reconstructed stacks of greyscale TIFF images into Drishti software (available at <https://sf.anu.edu.au/Vizlab/drishti/>). The greyscale value of each voxel is a function of X-ray attenuation, which varies due to density and atomic number. Inclusions are distinguishable from olivine because they have contrasting densities—fluid and spinel inclusions have lower and higher densities, respectively, than olivine. Sparse melt inclusions tend to be heterogeneous and have greyscale values that overlap with those of the host olivine, inhibiting precise measurement. We carried out volume analysis with Blob3D software (available at <http://www.ct-lab.geo.utexas.edu/software/blob3d/>) in this order: (1) removal of interstitial air volumes below the greyscale threshold of olivine, (2) separation of fluid inclusion volumes greater than six contiguous voxels below the greyscale threshold of olivine, and (3) separation of olivine volumes with intermediate greyscale values. The smallest inclusions distinguishable from signal noise are three voxels across, so the smallest detectible inclusions were 21–23  $\mu\text{m}$  in diameter.

Using Blob3D software, we calculated the volume, location, and dimensions of each separated component (fluid inclusions and olivine). Selecting greyscale thresholds involves a degree of subjectivity. Misassignment of thresholds can occur because greyscale values smear across inclusion contacts and is referred to as the partial volume effect, or PVE (Ketcham, 2005). In our dataset, PVE smearing is generally limited to three voxels on either side of fluid inclusion contacts. To quantify the effects of PVE, we used Blob3D to calculate PVE-corrected volumes (Ketcham, 2005). The PVE-corrected volumes are on average 7% smaller than uncorrected volumes, probably because smearing is most pronounced within the inclusions. We conservatively assign uncertainties equal to the difference between the PVE-corrected and uncorrected volumes for each inclusion.

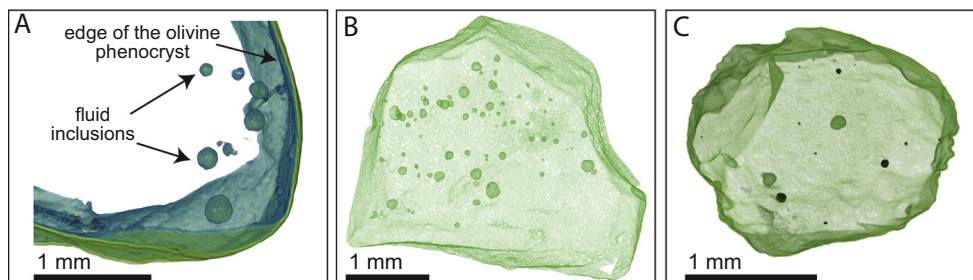


Fig. 1. X-ray computed tomography (microCT) reveals fluid inclusions in olivines. (A) A 3-D reconstruction of an olivine section containing several inclusions. (B) A representative example of an inclusion-rich olivine. (C) An example of an olivine that contains both spinel (black) and fluid (dark green) inclusions. (For interpretation of the references to colour in this figure legend, the reader is referred to the web version of this article.)

By summing the tomography-based fluid inclusion volumes in each grain, we ranked olivines by total fluid inclusion volume and selected 157 grains with the greatest inclusion volumes for further analysis. We crushed individual grains under vacuum using a newly developed stainless-steel crushing apparatus attached to a capacitance manometer and the noble gas mass spectrometer. In this device, a 5 mm metal slug applies pressure via manual rotation of the handle of a repurposed Nupro valve assembly to an olivine crystal lying at the bottom of a stainless-steel well. The operator turns the valve handle until the olivine is heard to crush.

CO<sub>2</sub> released during crushing rapidly adsorbs to fresh mineral surfaces created by crushing (e.g., [Barker and Torkelson, 1975](#)). To minimize this effect, we trapped the extracted CO<sub>2</sub> on a stainless-steel finger held at liquid nitrogen temperature before isolating the finger from the crushing chamber and releasing the gas into a Baratron capacitance manometer at room temperature. More than 97% of gas released by crushing froze down on the finger during each extraction, suggesting that inclusions contained <3% non-condensable gases, such as N<sub>2</sub>, CH<sub>4</sub>, and light noble gases. Except in cases when crushing yielded negligible signal on the manometer, the extracted gases were sequentially exposed to SAES getters for purification and adsorbed at 14 K onto charcoal in a cryogenic cold trap before being released at 34 K into a MAP 215-50 mass spectrometer for analysis of <sup>3</sup>He and <sup>4</sup>He. Isotope ratios were determined by comparison to the 16.45 Ra MM standard from Yellowstone National Park following the usual procedures at Caltech ([Patterson et al., 1997](#); [Patterson and Farley, 1998](#); [Mukhopadhyay et al., 2003](#)). He concentrations were determined by peak-height comparison to a standard with a manometrically determined He abundance. He crusher blanks were measured just prior to sample crushing and were <0.02 ncc. This amount was always negligible and no blank correction was required or made. Uncertainties were count-limited on <sup>3</sup>He and calculated based on the reproducibility of standard splits similar in size to each unknown.

### 3. RESULTS

#### 3.1. Inclusion and gas distributions

To our knowledge, no study characterizing the fluid inclusion distribution in a population of magmatic olivines has yet been published, so here we describe our results in some detail. The 1065 olivine crystals scanned with microCT have volumes ranging from 0.03 to 8 mcc (10<sup>-3</sup> cm<sup>3</sup>) and a mean volume of 1.1 mcc ([Fig. 2A](#)), which corresponds to a mean diameter of 1.3 mm assuming spherical geometry. Only 40% of these olivines have one or more identifiable fluid inclusions. The 1691 inclusions we detected have a mean aspect ratio of 1.55, and many of the larger inclusions appear nearly spherical in microCT projections ([Fig. 1](#)). Inclusion diameters range from the detection limit of ~20 μm (3 ncc) to 200 μm (4300 ncc) and have a mean diameter of 57 μm ([Fig. 2B](#)). Inclusions are exponentially more abundant with decreasing size down to the detection limit. Half of the inclusions are <45 μm in

diameter, but despite their abundance these smaller inclusions make up only 11% of the total inclusion volume. In contrast, inclusions 45–90 μm in diameter make up 52% of the total volume. On average, inclusions constitute 0.03% of olivine volume and up to ~0.5% in several cases ([Fig. 2C](#)). The mean number of inclusions per grain is four and 90% of the olivines have less than seven inclusions ([Fig. 2D](#)). The maximum number of fluid inclusions observed in a single olivine is 185. In general, inclusions tend to cluster towards the interior of grains and are not in planar arrays.

The mean CO<sub>2</sub> contents of the 157 crushed olivines is 1.7 × 10<sup>-9</sup> moles and ranges from below detection up to 2.6 × 10<sup>-8</sup> moles ([Fig. 2E](#)). Of these olivines, 112 were analyzed on the mass spectrometer, yielding He contents ranging from our detection limit of 0.02 ncc up to 53 ncc and averaging 2.78 ncc ([Fig. 2F](#)). The most inclusion-rich olivine by volume and number of inclusions yielded 53 ncc of He, which corresponds to >4000 ncc/g. For comparison, typical OIB olivines have He concentrations in the range of a few to a few tens of ncc/g. Of the olivines analyzed by mass spectrometry, the 5% with highest inclusion volumes yielded half of the total He, while the top 20% yielded 80% of the total He. These same olivines contained a smaller fraction of the CO<sub>2</sub>: the top 5% grains by inclusion volume yielded only ~20% of the total CO<sub>2</sub> released.

Olivines with the highest total inclusion volumes tend to have moderate diameters of 1–1.5 mm ([Fig. 3A](#)) and many fluid inclusions ([Fig. 3B](#)). For olivines with high inclusion volumes, inclusion volume generally corresponds with higher He content ([Fig. 3C](#)), but there are several olivines with exceptionally low He contents (<2 ncc) despite having high inclusion volumes (>1 μcc). No apparent correlation exists between CO<sub>2</sub> and inclusion volume. For example, olivines that released >5 × 10<sup>-9</sup> moles of CO<sub>2</sub> upon crushing have inclusion volumes that vary from 0.1 to 152 μcc ([Fig. 3D](#)).

#### 3.2. Helium isotopic compositions

In many cases, crushing of individual olivines yielded sufficient He to obtain reasonably precise He isotopic ratios ([Fig. 4](#)). The mean 2σ uncertainty of all single-grain analyses is 4.6 Ra, but each basalt has at least one single-crystal analysis with an uncertainty less than 2.5 Ra. In some cases, we achieved even better precision. For example, the most He-rich grain in the entire population has an uncertainty of 0.9 Ra. For the most part, olivines from the same basalt have homogeneous He isotopic compositions to within 2σ uncertainty. Grain 67 in sample Ofu-05-18 is a notable exception with a ratio of 15 Ra, well below the rest of the olivines from that basalt that average about 35 Ra. The reason for this discrepancy is not known, although it is notable that this grain has the lowest He yield for this basalt. Several Ofu-05-23 analyses also scatter a few Ra below the weighted mean for that basalt. Among basalts, He isotopic compositions vary by more than 10 Ra: the error-weighted means for two samples (Ofu-05-09 and Ofu-05-28) are 21 Ra, for five samples (Ofu-05-10, Ofu-05-13, Ofu-05-15, Ofu-05-16, Ofu-05-23) are ~30 Ra, and for a single sample

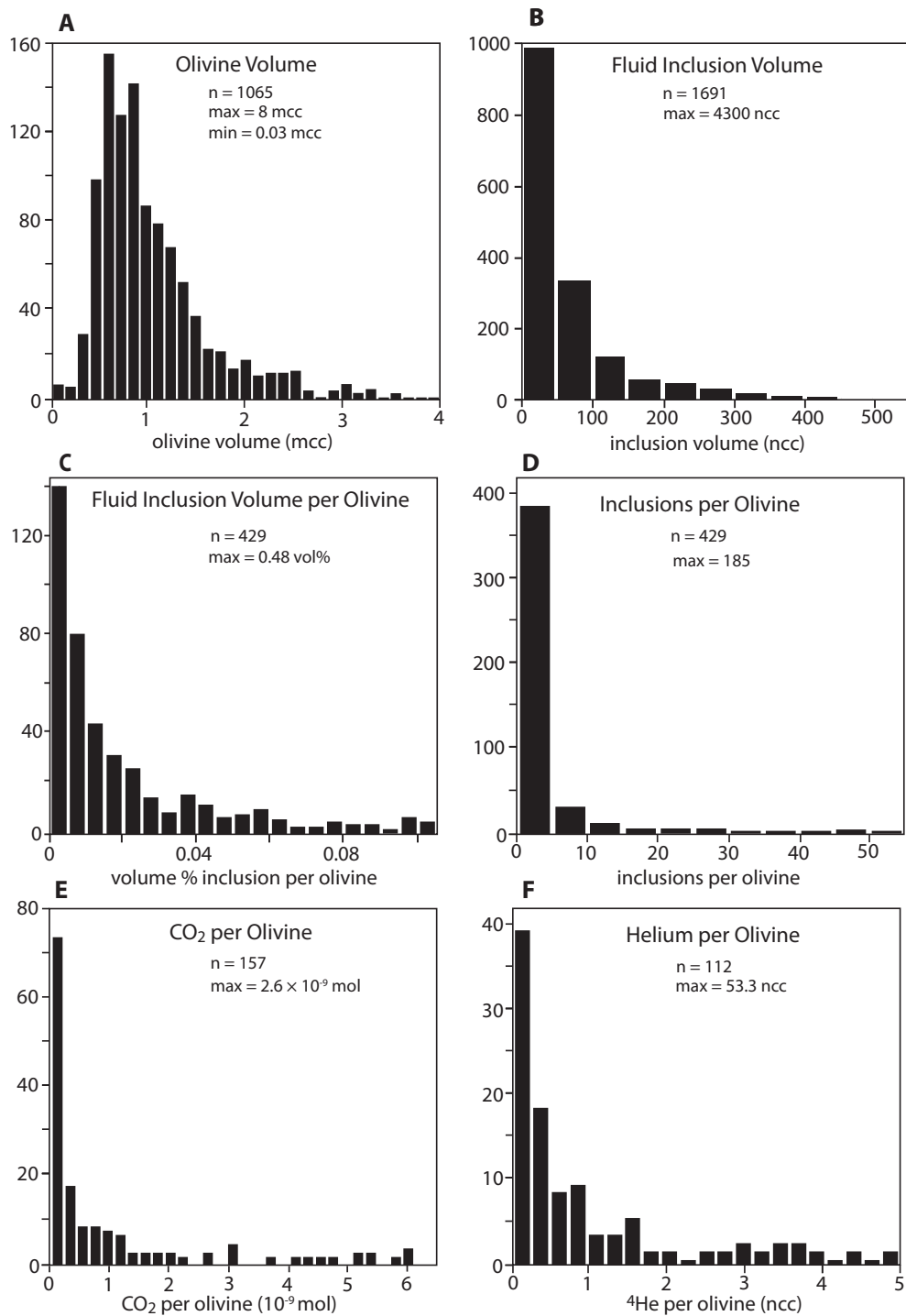


Fig. 2. Histograms showing the size and distributions of olivines and their fluid inclusions. Note that, in each case, the x-axis range truncates the data.

(Ofu-05-18) is 35 Ra. These ratios do not correlate with He content, CO<sub>2</sub> content, average inclusion size, or total inclusion volume. Nor is there any indication that the two unshielded samples (Ofu-05-23 and Ofu-05-28) have higher ratios associated with possible cosmic ray irradiation.

### 3.3. Barometry

Internal pressures in fluid inclusions potentially preserve information about the depths at which olivines entrained volatiles. To compute internal pressures, we need the molar

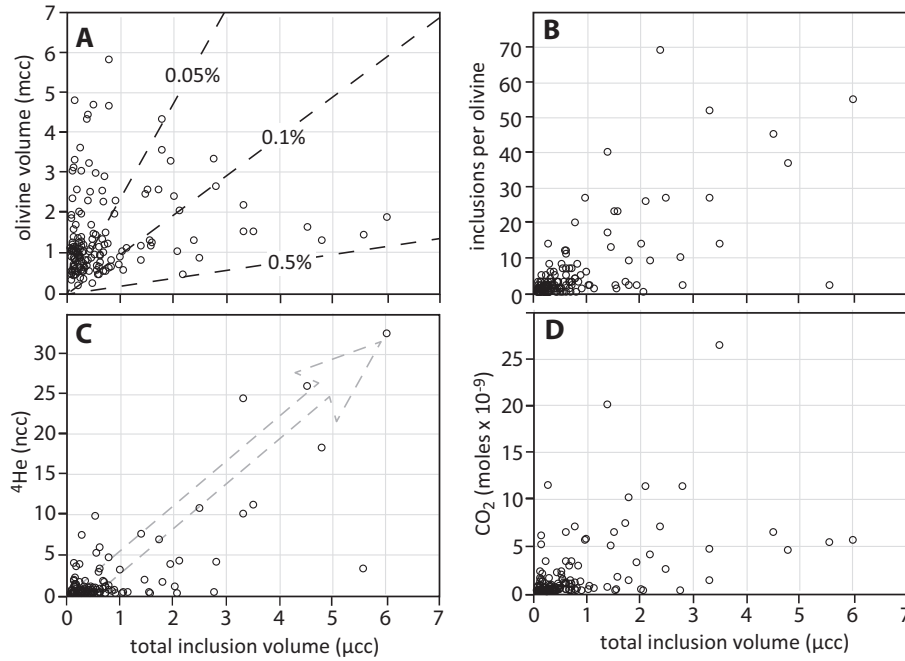


Fig. 3. The total fluid inclusion volume vs. (A) olivine volume, (B) the number of inclusions per olivine, (C)  $^4\text{He}$  contents, and (D)  $\text{CO}_2$  contents. Dashed lines in (A) reflect volume percentages of olivines that are inclusions. Higher  $^4\text{He}$  content generally corresponds (dashed arrow) with higher total inclusion volume for the most  $^4\text{He}$ -rich olivines.

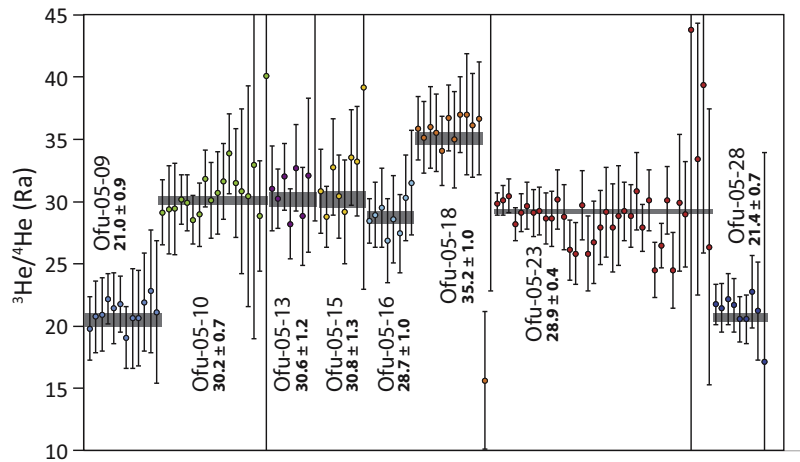


Fig. 4.  $^3\text{He}/^4\text{He}$  compositions of individual olivine crystals sorted by sample number and then in order of descending He content. Error bars are  $2\sigma$  uncertainties for single-grain analyses and the grey bars are the  $2\sigma$  uncertainty of the error-weighted mean for each sample. Note that the Ofu-05-18 is a sample taken from the same dike as Ofu-04-06 reported in [Jackson et al. \(2007\)](#), which yielded a  $^3\text{He}/^4\text{He}$  of  $33.8 \pm 0.4$  Ra ( $2\sigma$ ) in a bulk crushing experiment.

volume of the fluid in the fluid inclusions. Based on the moles of gas released during crushing each olivine and the total fluid inclusion volume per olivine measured via microCT, we can estimate the molar volume at room temperature. Under magmatic conditions,  $\text{CO}_2$  behavior is non-ideal, so we use the CORK equation of state ([Holland and Powell, 1991](#)) to calculate pressures over a range of magmatic temperatures (1100–1400 °C). This approach assumes that all the fluid inclusions observed with

microCT ruptured during crushing and that the released gases resided exclusively in these inclusions. To estimate pressure, we assume that the gas released from inclusions is entirely  $\text{CO}_2$ ; although we cannot rule out the presence of  $\text{H}_2\text{O}$  and observe up to 3%  $\text{N}_2$  or some other noncondensable gas, most fluid inclusions in OIB olivine are nearly pure  $\text{CO}_2$  (e.g., [Roedder, 1983](#); [Hansteen et al., 1998](#)). We further assume that inclusions did not host carbonate minerals. Although no mineral precipitates on inclusion walls

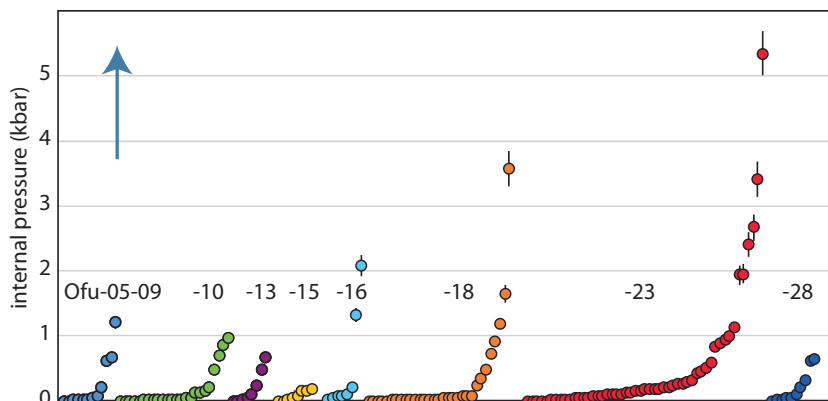


Fig. 5. Fluid inclusion pressures in individual olivines at  $1300 \pm 100$  °C based on inclusion volumes and the  $\text{CO}_2$  released during crushing. Analyses are ordered by sample number (Ofu-05-09 to Ofu-05-28 from left to right) and within each basalt by ascending mean internal pressure. Note that grains 63 and 65 in sample Ofu-05-09 have pressures of  $12.6 \pm 0.3$  kbar and  $22.5 \pm 0.8$  kbar, respectively, and are outside the bounds of this plot.

are detectable in the microCT data, the existence of carbonate mineralization similar to that observed on the walls of melt inclusion bubbles ( $<2$   $\mu\text{m}$  thick and constituting 0.1–1% of bubble volume: Moore et al., 2015) cannot be ruled out.

Two olivines we crushed yielded traces of  $\text{CO}_2$  (2–5  $\mu\text{cc}$ ) even though they lacked identifiable fluid inclusions. The other 155 crushed olivines have room temperature  $\text{CO}_2$  densities of  $6 \times 10^{-4}$  to  $1.4$   $\text{g}/\text{cm}^3$  and a mean density of  $0.08$   $\text{g}/\text{cm}^3$ . At  $1300$  °C, these densities correspond to average internal pressures per grain of 0.01–22.5 kbar and a mean pressure for all analyzed olivines of 0.5 kbar (Fig. 4). Analytical uncertainties for these pressures are on average 11%. These pressure estimates are relatively insensitive to magmatic temperature: magmatic conditions that were higher or lower by  $100$  °C would correspond to internal pressures that lower or higher, respectively, by 4–10%. In each basalt,  $\sim 60\%$  of the grains have pressures  $<0.1$  kbar, with the exception of Ofu-05-23 for which this majority is  $<0.2$  kbar. Each sample except for Ofu-05-15 contains high-pressure outliers. The most significant outliers in this regard are grains 63 and 65 in sample Ofu-05-09, for which we calculate pressures of  $12.6 \pm 0.3$  kbar and  $22.5 \pm 0.8$  kbar, respectively. Every sample except Ofu-05-15, however, has at least one olivine with pressure greater than or equal to 0.5 kbar.

### 3.4. Carbon-to-helium ratios

The 112 crushed olivines for which we measured both  $\text{CO}_2$  and He have a mean  $\text{C}/^3\text{He}$  of  $1.1 \times 10^9$  and a range of  $3.6 \times 10^7$ – $1.5 \times 10^{10}$  (Fig. 6A). The minima for the basalt dikes ( $1.2$ – $3.5 \times 10^8$ ) are slightly higher than the lowest ratio measured in the non-dike sample Ofu-05-23 ( $3.6 \times 10^7$ ). Means for each basalt are between  $6.1 \times 10^8$  and  $2.6 \times 10^9$ . The  $\text{C}/^3\text{He}$  of olivines within each basalt vary by approximately 0.5 to 2 orders of magnitude, which is greater than the differences among basalt means. Most of the analyses in each basalt have a roughly normal distribution (Fig. 6B) around a mean of  $\sim 10^9$ , but Ofu-05-23 has a

broader distribution between  $10^8$  and  $10^9$  and several outliers in both directions.

## 4. DISCUSSION

### 4.1. Grain-scale gas distributions

Fluid inclusions are increasingly abundant with decreasing size (Fig. 2B) and trails of inclusions below our microCT detection limit are visible with an optical microscope (Fig. 7A and B), suggesting that many small fluid inclusions went undetected. Nevertheless, intermediate sized inclusions constitute the majority of the total inclusion volume, indicating that we likely measured most of the inclusion volume in each basalt. We find that a small fraction of the olivines host the vast majority of the inclusions, while most olivines contain no detectable inclusions at all. The inclusion-rich olivines generally contain the highest He contents, confirming that fluid inclusions are the dominant repositories of He in OIB olivine. For these reasons, microCT analysis shows promise as a way of identifying olivines with high He contents *a priori*. Selecting these olivines for noble gas isotopic analysis can result in greater analytical precision for mantle-derived gas measurements and can enable the analysis of individual grains. It could also, in principle, be used to reject fluid-inclusion-rich grains when seeking to measure matrix-hosted cosmogenic  $^3\text{He}$ .

### 4.2. Inclusion pressures

The internal pressures calculated for individual olivines (Fig. 5) are unlikely to be solely a function of entrapment depth. Olivine precipitation and fractionation in Réunion magmas probably occurred at  $\sim 4$ – $8$  kbar (Albarède et al., 1997), and olivine growth probably occurs at similar pressures in most mantle magmas as they ascend (O'hara, 1968). Therefore, the two exceptionally high internal pressures (12.6 and 22.5 kbar) calculated for Ofu-05-09 olivines are probably not entrapment pressures. Both grains

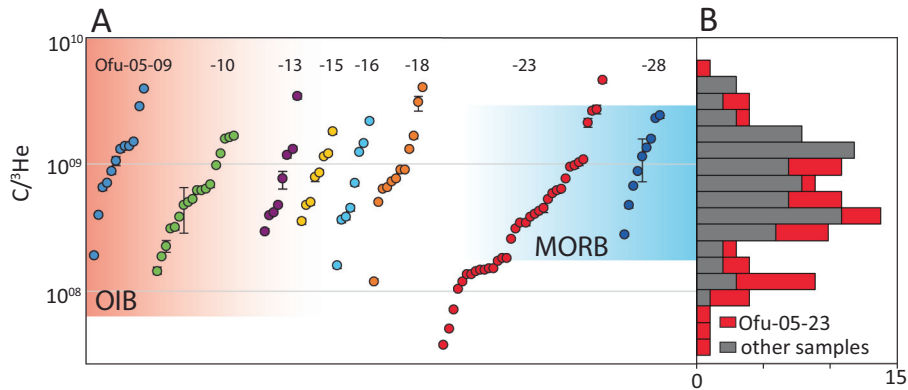


Fig. 6. (A)  $C/{}^3\text{He}$  ratios of individual olivines. Variability among olivines in individual basalt samples is comparable to the variability among global mid ocean ridge basalts (MORB, blue shading; [Marty and Zimmermann, 1999](#)) and ocean island basalt (OIB) seafloor vents (pink shading; [Hilton et al., 1998](#)). One data point from Ofu-05-18 (orange) falls off the plot at  $1.5 \times 10^{10}$ . (B) Histogram of  $C/{}^3\text{He}$  results with sample Ofu-05-23 plotted in red and the other Ofu samples plotted in grey. (For interpretation of the references to colour in this figure legend, the reader is referred to the web version of this article.)

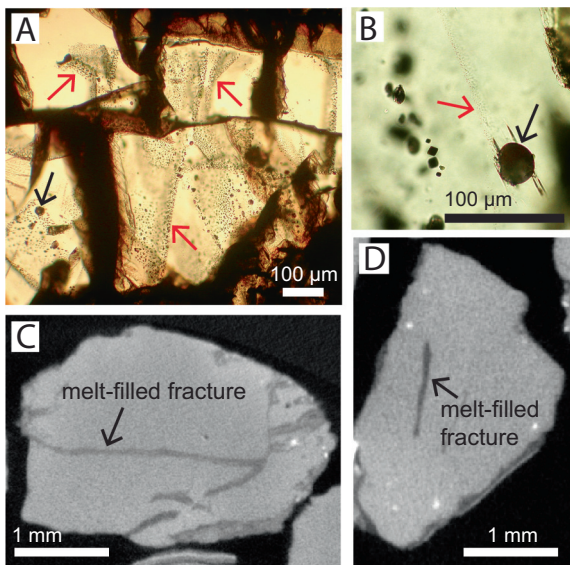


Fig. 7. (A) Primary fluid inclusions and abundant secondary inclusion trails similar to those described by [Roedder \(1983\)](#) are visible under an optical microscope in inclusion-rich olivines. Shown here is an example from Ofu-05-23. The inclusions in the trails were below the detection limit during microCT analysis. (B) Some primary inclusions (black arrows) have associated fractures and inclusion trails (red arrows) indicative of decrepitation. Several olivine crystals also contain melt-filled fractures (C and D), some of which reach the edge of the grain. These two olivines (C, Ofu-05-09 grain 63; D, Ofu-05-18 grain 67 in D) have especially high  $\text{CO}_2$  contents and high  $C/{}^3\text{He}$ , suggesting that melt fractures retain  $\text{CO}_2$  but not He, perhaps because He readily diffuses out through these melt channels. (For interpretation of the references to colour in this figure legend, the reader is referred to the web version of this article.)

contained anomalous melt-filled fractures ([Fig. 7C and D](#)), which may have hosted  $\text{CO}_2$  that skewed pressure estimates upward. Another source of error is the  $\text{CO}_2$  hosted by undetectably small inclusions, but as noted above these

probably constitute a minority of the inclusion volume. In contrast, more than 75% of the olivines have far lower pressures of  $<0.3$  kbar, which could in part reflect inclusion entrapment at  $<1$  km depth during olivine growth in the A'ofa caldera magma chamber ([Stice and McCoy, 1968](#)). However, the existence of abundant fluid inclusion trails leading away from larger inclusions ([Fig. 7A and B](#)) suggests that many inclusions lost  $\text{CO}_2$  after entrapment.

The inclusion trails we observe are indicative of decrepitation (i.e., fracturing of the host mineral) caused by the buildup of inclusion overpressure relative to the exterior of the grain during olivine ascent in a magma ([Roedder, 1983](#); [MacLennan, 2017](#)). If decrepitation fractures reach the edge of the grain, inclusions presumably lose  $\text{CO}_2$  to the surrounding melt. Fractures can anneal rapidly under magmatic conditions ([Wanamaker et al., 1990](#)), such that overpressures will begin increasing again in decrepitated inclusions if their host olivine continues to ascend. The overpressure necessary to cause decrepitation depends on a number of factors, including inclusion radius, inclusion distance from the grain edge, temperature, and ductile deformation rates within the olivine. Based on experimental stretching ([Wanamaker and Evans, 1989](#)) and decrepitation ([Wanamaker et al., 1990](#)) constraints, we designed a forward model to predict the effects of decrepitation for several of the inclusion-rich olivines we analyzed (See [supplementary material](#) for model details). We calculate that inclusions  $>20$   $\mu\text{m}$  across (i.e., all inclusions detectable in this study) are unstable at overpressures above 2 kbar under magmatic conditions. Predicted maximum pressures for individual olivines in our suite are even lower—0.2–0.6 kbar—because they host larger inclusions able to withstand less overpressure. The observed pressure range in our measured fluid inclusions ([Fig. 4](#)) is much broader and extends to both higher and lower pressures than the decrepitation model predicts. Lower than expected pressures might reflect entrapment during shallow olivine growth. Alternatively or in addition, decrepitation might have compromised the tensile strength of the olivine along

fracture planes, allowing for subsequent decrepitation at lower overpressures. We cannot distinguish between these potential causes of the pressure variations we observe. Nevertheless, our results highlight the fact that complex sub-grain mineral mechanics control the CO<sub>2</sub> retention—and thus filling pressure—in olivine-hosted fluid inclusions.

#### 4.3. Helium diffusion and C<sup>3</sup>He ratios

Variability in C<sup>3</sup>He ratio among individual fluid inclusions in a dunite xenolith (Burnard et al., 1994) and among magmatic olivine crystals (Fig. 6) indicates that He decouples from C at the grain scale. Closed system degassing of magmas produces limited C-He fractionation: although He is slightly more soluble in basaltic melts than C, the C<sup>3</sup>He ratio in vesicles can vary at most by a factor of ~2.5 during closed system degassing (Bottinga and Javoy, 1990; Hilton et al., 1998). Open system degassing of magmas (Rayleigh distillation) can have a greater effect. For equilibrium Rayleigh distillation, the C<sup>3</sup>He in a magma can be expressed as a function of the initial ratio, denoted by subscript 0, and fraction of C remaining,  $f_C$ :

$$\frac{C}{^3\text{He}} = \left( \frac{C}{^3\text{He}} \right)_0 \times f_C^{(1-\alpha)}$$

where  $\alpha$  is the ratio of C-to-He solubility (~0.5) in the melt (Tucker et al., 2018). Thus, ~99% CO<sub>2</sub> loss from a degassing magma could fractionate C<sup>3</sup>He by a factor of 10. Disequilibrium Rayleigh distillation (i.e., diffusion-limited gas loss from magma: Gonnermann and Mukhopadhyay, 2007) suppresses C<sup>3</sup>He because CO<sub>2</sub> has lower diffusivity in magmas than He (Tucker et al., 2018), so even greater CO<sub>2</sub> loss is probably necessary to cause order-of-magnitude fractionation in natural systems. Although >99% C loss from OIB magmas is conceivable, the preservation of C<sup>3</sup>He ratios from such a wide range of degassing stages seems unlikely, especially in olivines from individual samples. Thus, fluid inclusion entrapment (and/or reequilibration via decrepitation) during various stages of degassing can explain some—but probably not all—of the nearly two orders of magnitude C<sup>3</sup>He variability observed in the Samoan olivines we studied.

Here we consider an additional or alternative explanation that can simultaneously account for (a) the large C<sup>3</sup>He variability among the olivines and (b) the observation that high inclusion volume often corresponds with <sup>4</sup>He abundance (Fig. 3). In particular, we consider the possibility that diffusion allows He in the fluid inclusions to equilibrate with the evolving He partial pressure in the host magma as the magma ascends and experiences open system degassing.

Based on the He diffusivity data of Blard et al. (2008), at magmatic temperatures the time-scale ( $t = x^2/D$ ) for He diffusion through the matrix of a 5 mm inclusion-free olivine is just 15 years. However, step-heating experiments indicate that He loss from olivines with fluid inclusions is impeded relative to matrix diffusion (Hart, 1984; Trull and Kurz, 1993). This arises from the fact that the rate of He exchange between inclusions and grain exteriors depends on He diffusion rates and He solubility in olivine

(Trull and Kurz, 1993). Still, these experiments suggest that significant diffusive exchange between fluid inclusions and grain exteriors occurs at or near basalt solidus temperatures: the time-scale of He diffusion out of a 5 mm inclusion-bearing olivine would slow from 50 to 600 years as it cools from 1200 °C to 1100 °C. Diffusive exchange would equilibrate the partial pressure of He in fluid inclusions with the partial pressure of He in the enclosing magma as it outgasses. This offers an obvious explanation for the observation that greater inclusion volume corresponds with <sup>4</sup>He abundance (Fig. 3C): regardless of initial filling pressure or decrepitation, the He partial pressure in the inclusions remains in equilibrium with the exterior of the olivine at temperatures that cause rapid exchange. This line of reasoning implies that preserved internal He pressures reflect the partial pressure of He in the host magma when the system closed to He diffusion. Thus, greater inclusion volume means more He; a linear approximation of this trend in Fig. 3C has a positive slope of  $\sim 5.5 \times 10^{-3}$ . Based on this relationship and assuming Henry's Law constants from Jambon et al. (1986) and Lux (1987), magma in equilibrium with the He-rich olivines at 1200 °C would contain  $\sim 10^{-10}$  cc <sup>3</sup>He/g. This is less than thought to exist in most mid-ocean ridge samples ( $\sim 4 \times 10^{-10}$  cc/g; Porcelli and Ballentine, 2002) and among the highest amounts found in submarine OIB glasses (approximately  $10^{-11}$  to  $10^{-10}$  cc/g; Gonnermann and Mukhopadhyay, 2007).

Diffusive exchange of He may also maintain isotopic equilibrium between the fluid inclusions and the magma. It is interesting to speculate that this phenomenon allows He in olivine-hosted fluid inclusions to equilibrate with their host magma regardless of whether the olivines are cogenetic with that magma. This has obvious implications for the correlation of olivine-hosted He isotope ratios with lithophile isotope tracers (Sr, Nd, Pb, etc.) carried in the host magma; indeed, the lithophile tracers in Samoan magmas often do not reflect the compositions of their olivine cargo, which indicates He decoupling from Sr-Nd-Pb at the scale of melt inclusions (Reinhard et al., 2016). Diffusive exchange of He also raises the possibility of decoupling of He from the heavier noble gases if the diffusivity of Ne-Ar-Kr-Xe through olivine does not keep pace with He. Further work on noble gas diffusion through inclusion-bearing olivine is necessary to quantitatively assess this possibility.

When magmas fully outgas, the ambient He partial pressure plummets and He diffuses out of olivines unless they cool rapidly (e.g., Hart, 1984). Assuming the Ofu-Olosega dike magmas remained vapor saturated until emplacement, the ambient He partial pressure in the magmas probably prevented substantial He diffusion out of olivines until the dikes crystallized. The amount of post-crystallization He loss depends on the temperature at which the magma outgassed and the cooling rate. Based on cooling rates published by Jaeger (1957) and diffusion rates determined by Trull and Kurz (1993), we model He loss from spherical olivines in terms of outgassing temperature and dike thickness (See Supplementary Information). If the center of the 1-meter-thick dike cools at 20,000 °C/yr and the partial pressure of He drops to zero at <1200 °C due to open-system outgassing, olivines throughout the dike retain

>90% of their initial He contents (Fig. S2). Fluid inclusions near grain boundaries will theoretically lose He fastest, so variable He partial pressures in olivines might reflect variable degrees of He loss. This can account for deviations from the general trend in Fig. 3C.

Subaerial flows can cool more slowly than dikes, depending on the flow rate, the extent of stirring, and the amount of rainfall. With low viscosities that allow for efficient stirring, open channel Hawaiian flows cool at  $\sim 150,000$  °C/yr (Cashman et al., 1999) until lavas crystallize. In contrast, Columbia River basalt flows that are tens of meters thick cool as slowly as 2 °C/yr in the center of the flows and up to 20,000 °C/yr near the top where rainwater speeds cooling (Long and Wood, 1986). Olivines near the middle of such flows may lose half or more of the He trapped in fluid inclusions. For comparison, submarine basalt flows can cool more than an order of magnitude faster than dikes and subaerial flows (Coish and Taylor, 1979; Bowles et al., 2005), so olivines in submarine basalts should be more He retentive.

He equilibration can also explain the extremely variable  $C/{}^3\text{He}$  ratios we observe. The diffusivity of C through olivine at magmatic temperatures (Tingle et al., 1988) is at least 3 orders of magnitude slower than He. Thus, unlike He,  $\text{CO}_2$  in inclusions only exchanges during decrepitation events. He diffusion out of inclusions increases inclusion  $C/{}^3\text{He}$  ratios. Because magmatic degassing will drive He diffusion out of olivines, we expect that magmas initially had  $C/{}^3\text{He}$  ratios less than or equal to the lowest  $C/{}^3\text{He}$  ratios observed in our olivines. For the dike samples, this implies an initial  $C/{}^3\text{He}$  ratios no higher than  $1\text{--}4 \times 10^8$ , which is slightly less than the lowest ratios measured in Loihi seafloor vents ( $5.9 \times 10^8$ ; Hilton et al., 1998) and vesicles in Iceland volcanic glass ( $6.7 \pm 0.5 \times 10^8$ ; Colin et al., 2015). This result implies primary magmatic  $C/{}^3\text{He}$  ratios substantially lower than previous estimates for high  ${}^3\text{He}/{}^4\text{He}$  hotspot magmas based on OIB xenoliths ( $1\text{--}20 \times 10^9$ ; Trull et al., 1993; Burnard et al., 1994), submarine glass ( $10^{10}$ ; Peterson et al., 2017), submarine glass vesicles ( $\sim 2 \times 10^9$ ; Péron et al., 2016), and geothermal springs in Iceland ( $10^9$  to  $10^{10}$ ; Poreda et al., 1992). Thus, the  $C/{}^3\text{He}$  ratio of OIB mantle material may be lower than previous studies suggest.

If the  $C/{}^3\text{He}$  ratio in the depleted upper mantle increases over time due to preferential C retention during ridge spreading and preferential C recycling during subduction because  ${}^3\text{He}$  is lost to space, we might expect OIB sourced from the deep mantle to have lower  $C/{}^3\text{He}$  than MORB ( $\sim 2 \times 10^9$ ; Marty and Jambon, 1987; Tucker et al., 2018). Indeed, our results are consistent with this scenario. Complex explanations for the lack of C-He fractionation during melt extraction from—and subduction into—the upper mantle (e.g., Marty and Jambon, 1987; Trull et al., 1993) are unnecessary. Furthermore, this result lends credence to the existence of mantle reservoirs with  $C/{}^3\text{He}$  compositions approaching that of enstatite chondrite (Marty and Zimmermann, 1999) that have not been replenished by recycled carbon (e.g., Colin et al., 2015). In these respects, our results help reconcile global volatile flux estimates with the existence of a less degassed deep mantle reservoir.

## 5. CONCLUSIONS

This study provides insight about the distribution and mobility of volatiles in olivines. Most fluid inclusions—the primary hosts of  $\text{CO}_2$  and He in olivine—are concentrated in a small fraction of the olivines. We find evidence for ubiquitous fluid inclusion decrepitation, suggesting that inclusion-hosted volatiles generally do not correspond to the conditions of olivine growth. We also observe grain-scale decoupling of C and He, which we attribute to He diffusion through the olivine lattice. Based on our analysis, the conditions that favor high He concentrations in olivine include (i) voluminous cavities in the crystals, (ii) high He partial pressures sustained in host magmas until eruption or emplacement, and (iii) rapid cooling. Because all three conditions are seldom met in nature, the  $C/{}^3\text{He}$  and He concentrations measured in OIB olivines are generally not representative of their host magmas.

## ACKNOWLEDGEMENTS

This research was supported by NSF award number 1650308. We thank the members of the X-ray CT Facility at University of Texas Austin; William Carlson and Jessica Maisano, in particular, provided crucial assistance and advice. A thorough review by Jonathan Tucker improved this manuscript, as did two anonymous reviews.

## APPENDIX A. SUPPLEMENTARY MATERIAL

Supplementary data to this article can be found online at <https://doi.org/10.1016/j.gca.2018.10.013>.

## REFERENCES

- Albarède F., Luais B., Fitton G., Semet M., Kaminski E., Upton B. G. J., Bachelery P. and Cheminée J.-L. (1997) The geochemical regimes of Piton de la Fournaise volcano (Réunion) during the last 530 000 years. *J. Petrol.* **38**, 171–201.
- Barker C. and Torkelson B. E. (1975) Gas adsorption on crushed quartz and basalt. *Geochim. Cosmochim. Acta* **39**, 212–218. [https://doi.org/10.1016/0016-7037\(75\)90173-8](https://doi.org/10.1016/0016-7037(75)90173-8).
- Blard P.-H., Puchol N. and Farley K. A. (2008) Constraints on the loss of matrix-sited helium during vacuum crushing of mafic phenocrysts. *Geochim. Cosmochim. Acta* **72**, 3788–3803. <https://doi.org/10.1016/j.gca.2008.05.044>.
- Bottinga Y. and Javoy M. (1990) MORB degassing: bubble growth and ascent. *Chem. Geol.* **81**, 255–270.
- Botz R., Winckler G., Bayer R., Schmitt M., Garbe-Schönberg D., Stoffers P. and Kristjansson J. K. (1999) Origin of trace gases in submarine hydrothermal vents of the Kolbeinsey Ridge, north Iceland. *Earth Planet. Sci. Lett.* **171**, 83–93.
- Bowles J., Gee J. S., Kent D. V., Bergmanis E. and Sinton J. (2005) Cooling rate effects on paleointensity estimates in submarine basaltic glass and implications for dating young flows. *Geochim. Geophys., Geosyst.* **6**.
- Burnard P. G., Stuart F. and Turner G. (1994) C-He-Ar variations within a dunite nodule as a function of fluid inclusion morphology. *Earth Planet. Sci. Lett.* **128**, 243–258.
- Cashman K. V., Thornber C. and Kauahikaua J. P. (1999) Cooling and crystallization of lava in open channels, and the transition of Pāhoehoe Lava to 'A'ā. *Bull. Volcanol.* **61**, 306–323.

- Coish R. A. and Taylor L. A. (1979) The effects of cooling rate on texture and pyroxene chemistry in DSDP Leg 34 basalt: a microprobe study. *Earth Planet. Sci. Lett.* **42**, 389–398.
- Colin A., Moreira M., Gautheron C. and Burnard P. (2015) Constraints on the noble gas composition of the deep mantle by bubble-by-bubble analysis of a volcanic glass sample from Iceland. *Chem. Geol.* **417**, 173–183. <https://doi.org/10.1016/j.chemgeo.2015.09.020>.
- Farley K. A., Basu A. R. and Craig H. (1993) He, Sr and Nd isotopic variations in lavas from the Juan Fernandez Archipelago, SE Pacific. *Contrib. Mineral. Petrol.* **115**, 75–87. <https://doi.org/10.1007/BF00712980>.
- Farley K. A. and Neroda E. (1998) Noble gases in the Earth's mantle. *Annu. Rev. Earth Planet. Sci.* **26**, 189–218.
- Gonnermann H. M. and Mukhopadhyay S. (2007) Non-equilibrium degassing and a primordial source for helium in ocean-island volcanism. *Nature* **449**, 1037.
- Graham D. W., Jenkins W. J., Schilling J.-G., Thompson G., Kurz M. D. and Humphris S. E. (1992) Helium isotope geochemistry of mid-ocean ridge basalts from the South Atlantic. *Earth Planet. Sci. Lett.* **110**, 133–147. [https://doi.org/10.1016/0012-821X\(92\)90044-V](https://doi.org/10.1016/0012-821X(92)90044-V).
- Graham D. W., Christie D. M., Harpp K. S. and Lupton J. E. (1993) Mantle Plume Helium in Submarine Basalts from the Galápagos Platform. *Science* **262**, 2023–2026. <https://doi.org/10.1126/science.262.5142.2023>.
- Hansteen T. H., Klügel A. and Schmincke H.-U. (1998) Multi-stage magma ascent beneath the Canary Islands: evidence from fluid inclusions. *Contrib. Mineral. Petrol.* **132**, 48–64.
- Hart S. R. (1984) He diffusion in olivine. *Earth Planet. Sci. Lett.* **70**, 297–302.
- Heber V. S., Brooker R. A., Kelley S. P. and Wood B. J. (2007) Crystal–melt partitioning of noble gases (helium, neon, argon, krypton, and xenon) for olivine and clinopyroxene. *Geochim. Cosmochim. Acta* **71**, 1041–1061. <https://doi.org/10.1016/j.gca.2006.11.010>.
- Hilton D. R., McMurtry G. M. and Goff F. (1998) Large variations in vent fluid CO<sub>2</sub>/He ratios signal rapid changes in magma chemistry at Loihi seamount, Hawaii. *Nature* **396**, 359.
- Holland T. and Powell R. (1991) A compensated-Redlich-Kwong (CORK) equation for volumes and fugacities of CO<sub>2</sub> and H<sub>2</sub>O in the range 1 bar to 50 kbar and 100–1600 C. *Contrib. Mineral. Petrol.* **109**, 265–273.
- Jackson M. G., Kurz M. D., Hart S. R. and Workman R. K. (2007) New Samoan lavas from Ofu Island reveal a hemispherically heterogeneous high <sup>3</sup>He/<sup>4</sup>He mantle. *Earth Planet. Sci. Lett.* **264**, 360–374.
- Jaeger J. C. (1957) The temperature in the neighborhood of a cooling intrusive sheet. *Am. J. Sci.* **255**, 306–318.
- Jambon A., Weber H. and Braun O. (1986) Solubility of He, Ne, Ar, Kr and Xe in a basalt melt in the range 1250–1600 C. *Geochem. Impl.: Geochim. Cosmochim. Acta* **50**, 401–408.
- Javoy M. and Pineau F. (1991) The volatiles record of a “popping” rock from the Mid-Atlantic Ridge at 14°N: chemical and isotopic composition of gas trapped in the vesicles. *Earth Planet. Sci. Lett.* **107**, 598–611. [https://doi.org/10.1016/0012-821X\(91\)90104-P](https://doi.org/10.1016/0012-821X(91)90104-P).
- Kendrick M. A., Jackson M. G., Hauri E. H. and Phillips D. (2015) The halogen (F, Cl, Br, I) and H<sub>2</sub>O systematics of Samoan lavas: assimilated-seawater, EM2 and high-<sup>3</sup>He/<sup>4</sup>He components. *Earth Planet. Sci. Lett.* **410**, 197–209.
- Ketchum R. A. (2005) Computational methods for quantitative analysis of three-dimensional features in geological specimens. *Geosphere* **1**, 32.
- Kurz M. D., Jenkins W. J. and Hart S. R. (1982) Helium isotopic systematics of oceanic islands and mantle heterogeneity. *Nature* **297**, 43–47.
- Kurz M. D., Jenkins W. J., Hart S. R. and Clague D. (1983) Helium isotopic variations in volcanic rocks from Loihi Seamount and the Island of Hawaii. *Earth Planet. Sci. Lett.* **66**, 388–406.
- Long P. E. and Wood B. J. (1986) Structures, textures, and cooling histories of Columbia River basalt flows. *Geol. Soc. Am. Bull.* **97**, 1144–1155.
- Lux G. (1987) The behavior of noble gases in silicate liquids: solution, diffusion, bubbles and surface effects, with applications to natural samples. *Geochim. Cosmochim. Acta* **51**, 1549–1560. [https://doi.org/10.1016/0016-7037\(87\)90336-X](https://doi.org/10.1016/0016-7037(87)90336-X).
- MacLennan J. (2017) Bubble formation and decrepitation control the CO<sub>2</sub> content of olivine-hosted melt inclusions. *Geochem. Geophys. Geosyst.* **18**, 597–616.
- Marty B. and Jambon A. (1987) C<sup>3</sup>He in volatile fluxes from the solid Earth: implications for carbon geodynamics. *Earth Planet. Sci. Lett.* **83**, 16–26.
- Marty B. and Lussiez P. (1993) Constraints on rare gas partition coefficients from analysis of olivine-glass from a picritic mid-ocean ridge basalt. *Chem. Geol.* **106**, 1–7.
- Marty B. and Zimmermann L. (1999) Volatiles (He, C, N, Ar) in mid-ocean ridge basalts: assesment of shallow-level fractionation and characterization of source composition. *Geochim. Cosmochim. Acta* **63**, 3619–3633.
- McDougall I. A. N. (2010) Age of volcanism and its migration in the Samoa Islands. *Geol. Mag.* **147**, 705–717.
- Moore L. R., Gazel E., Tuohy R., Lloyd A. S., Esposito R., Steele-MacInnis M., Hauri E. H., Wallace P. J., Plank T. and Bodnar R. J. (2015) Bubbles matter: an assessment of the contribution of vapor bubbles to melt inclusion volatile budgets. *Am. Mineral.* **100**, 806–823. <https://doi.org/10.2138/am-2015-5036>.
- Mukhopadhyay S., Lassiter J. C., Farley K. A. and Bogue S. W. (2003) Geochemistry of Kauai shield-stage lavas: Implications for the chemical evolution of the Hawaiian plume. *Geochem. Geophys. Geosyst.* **4**. <https://doi.org/10.1029/2002GC000342>.
- O'hara M. J. (1968) Are ocean floor basalts primary magma? *Nature* **220**, 683.
- Patterson D. B. and Farley K. A. (1998) Extraterrestrial <sup>3</sup>He in seafloor sediments: evidence for correlated 100 kyr periodicity in the accretion rate of interplanetary dust, orbital parameters, and Quaternary climate. *Geochim. Cosmochim. Acta* **62**, 3669–3682. [https://doi.org/10.1016/S0016-7037\(98\)00263-4](https://doi.org/10.1016/S0016-7037(98)00263-4).
- Patterson D. B., Farley K. A. and McInnes B. I. A. (1997) Helium isotopic composition of the Tabar-Lihir-Tanga-Feni island arc, Papua New Guinea. *Geochim. Cosmochim. Acta* **61**, 2485–2496. [https://doi.org/10.1016/S0016-7037\(97\)00095-1](https://doi.org/10.1016/S0016-7037(97)00095-1).
- Péron S., Moreira M., Colin A., Arbaret L., Putlitz B. and Kurz M. D. (2016) Neon isotopic composition of the mantle constrained by single vesicle analyses. *Earth Planet. Sci. Lett.* **449**, 145–154.
- Peterson M. E., Saal A. E., Kurz M. D., Hauri E. H., Blusztajn J. S., Harpp K. S., Werner R. and Geist D. J. (2017) Submarine basaltic glasses from the Galapagos Archipelago: determining the volatile budget of the mantle plume. *J. Petrol.* **58**, 1419–1450.
- Porcelli D. and Ballentine C. J. (2002) Models for Distribution of Terrestrial Noble Gases and Evolution of the Atmosphere. *Reviews in Mineralogy and Geochemistry* **47**, 411–480. <https://doi.org/10.2138/rmg.2002.47.11>.
- Poreda R. J., Craig H., Arnórsson S. and Welhan J. A. (1992) Helium isotopes in Icelandic geothermal systems: I. <sup>3</sup>He, gas chemistry, and <sup>13</sup>C relations. *Geochim. Cosmochim. Acta* **56**, 4221–4228. [https://doi.org/10.1016/0016-7037\(92\)90262-H](https://doi.org/10.1016/0016-7037(92)90262-H).

- Poreda R. J. and Farley K. A. (1992) Rare gases in Samoan xenoliths. *Earth Planet. Sci. Lett.* **113**, 129–144.
- Reinhard A. A., Jackson M. G., Harvey J., Brown C. R. and Koornneef J. M. (2016) Extreme differences in  $^{87}\text{Sr}/^{86}\text{Sr}$  between Samoan lavas and the magmatic olivines they host: evidence for highly heterogeneous  $^{87}\text{Sr}/^{86}\text{Sr}$  in the magmatic plumbing system sourcing a single lava. *Chem. Geol.* **439**, 120–131.
- Roedder E. (1983) Geobarometry of ultramafic xenoliths from Loihi Seamount, Hawaii, on the basis of  $\text{CO}_2$  inclusions in olivine. *Earth Planet. Sci. Lett.* **66**, 369–379. [https://doi.org/10.1016/0012-821X\(83\)90152-8](https://doi.org/10.1016/0012-821X(83)90152-8).
- Stice, G. D. and McCoy Jr, F. W. (1968) The geology of the Manu'a Islands, Samoa.
- Tingle T. N., Green H. W. and Finnerty A. A. (1988) Experiments and observations bearing on the solubility and diffusivity of carbon in olivine. *J. Geophys. Res.: Solid Earth* **93**, 15289–15304.
- Trull T. W. and Kurz M. D. (1993) Experimental measurements of  $^3\text{He}$  and  $^4\text{He}$  mobility in olivine and clinopyroxene at magmatic temperatures. *Geochim. Cosmochim. Acta* **57**, 1313–1324.
- Trull T., Nadeau S., Pineau F., Polve M. and Javoy M. (1993) C-He systematics in hotspot xenoliths: implications for mantle carbon contents and carbon recycling. *Earth Planet. Sci. Lett.* **118**, 43–64.
- Tucker J. M., Mukhopadhyay S. and Gonnermann H. M. (2018) Reconstructing mantle carbon and noble gas contents from degassed mid-ocean ridge basalts. *Earth Planet. Sci. Lett.* **496**, 108–119. <https://doi.org/10.1016/j.epsl.2018.05.024>.
- Wanamaker B. J. and Evans B. (1989) Mechanical re-equilibration of fluid inclusions in San Carlos olivine by power-law creep. *Contrib. Mineral. Petrol.* **102**, 102–111.
- Wanamaker B. J., Wong T.-F. and Evans B. (1990) Decrepitation and crack healing of fluid inclusions in San Carlos olivine. *J. Geophys. Res.: Solid Earth* **95**, 15623–15641.

Associate editor: Andreas Stracke